Ann. Phys. (Berlin) **18**, No. 10 – 11, 675 – 698 (2009) / **DOI** 10.1002/andp.200910367

Review Article

Thermal dynamics at surfaces

H. Brune*

Institute of Condensed Matter Physics, Ecole Polytechnique Fédérale de Lausanne (EPFL), 1015 Lausanne, Switzerland

Received 7 July 2009, accepted 26 August 2009 by U. Eckern
Published online 5 October 2009

Key words Surface diffusion, adatom gas, surface phonons, surface anharmonicity, surface melting, surface roughening, thermal surface reconstructions.
PACS 64.70.-p, 68.03.-g, 68.03.Cd, 68.08.-p, 68.08.Bc, 68.18.Jk

The present paper describes what happens at the surface of a crystal as its temperature steadily increases from zero Kelvin close to the bulk melting temperature. We treat thermal motion, such as the diffusion of individual adatoms establishing mass transport, the formation of adatom or vacancy gases coexisting with islands or steps of the condensed phase, surface phonons and the anharmonicity of the surface potential being markedly different from the one in bulk, as well as thermally induced reconstructions, surface roughening, and finally surface melting, which usually well precedes bulk melting. The paper intends to give an overview with references to the original and review literature.

1 Introduction

We briefly review phenomena involving thermally induced surface dynamics and present them in order of increasing onset temperature. One can situate them in a generic way on a temperature scale, when their onset temperature is expressed relative to the bulk melting temperature, T_{m}, see Fig. 1.

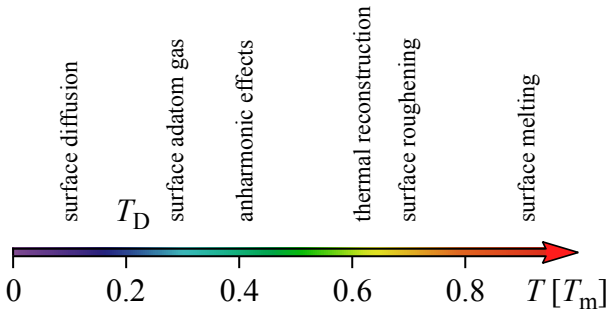

Fig. 1 (online colour at: www.ann-phys.org) The onset temperatures of thermally induced phenomena scaled to the bulk melting temperature, T_{m}. This generic scale is an approximation since some of the mentioned processes, e.g., thermal surface reconstructions may not exist for some systems, and the relative temperatures, in particular for surface diffusion, adatom or vacancy pair formation, may vary between surface orientations. T_{D} is the Debye temperature.

The process becoming activated at lowest temperatures is the diffusion of adatoms. The onset temperature refers to one atomic diffusion event per second and its value strongly depends on the crystal plane. For closed packed surfaces it can be as low as 1 % T_{m}, whereas it is of the order of 10 % T_{m} for self-diffusion on the more open surfaces, such as face-centered-cubic (fcc) (100). These onset temperatures refer to the case where isolated adatoms are present on the terraces, which is not the ground state. However, entropic

* E-mail: harald.brune@epfl.ch, Phone: +41 21 693 5451, Fax: +41 21 693 3603

reasons favor the creation of adatoms, and in some cases also of vacancies, so that the free energy gets lower when the atomic terraces are covered by a two-dimensional (2D) adatom or vacancy gas coexisting with the condensed phase. For many cases this happens at roughly 30 % T_{m}, earlier for open crystal planes and later for the close packed ones. This adatom or vacancy gas is very important as it establishes mass transport along concentration gradients, but it also changes the surface work function, and often is the source from which thermal evaporation of the crystal takes place. The anharmonicity of surface bonds may be different from the one in bulk. Surface anharmonicity leads to interlayer distances that vary with temperature in a different way (sign and amount) than the thermal expansion in bulk. It also leads to surface specific phonon dispersion relations.

The adatom gas, together with the temperature dependent surface interlayer distances, can drive surface reconstructions. Some of them appear at high temperature only, and fade away when the crystal is cooled down again. These are referred to in Fig. 1 as thermal reconstructions. At higher temperature the energies for the creation of steps may vanish when the crystal surface is in equilibrium with its three-dimensional (3D) vapor phase. Under these circumstances the surface free energies of all facets become equal, the characteristic mesoscopic low index facets delimiting crystals at low temperature disappear, and the surface roughens. Figure 2 shows hexagonal close-packed (hcp) ^{4}He crystals in equilibrium with their superfluid. They display facets at $T = 0.4$ K, as evident from clearly visible corners and edges [1]. These get rounded when the surface starts to roughen at 1.1 K until the crystal gets spherical at 1.4 K, minimizing the surface to volume ratio under the condition of isotropic surface free energies.

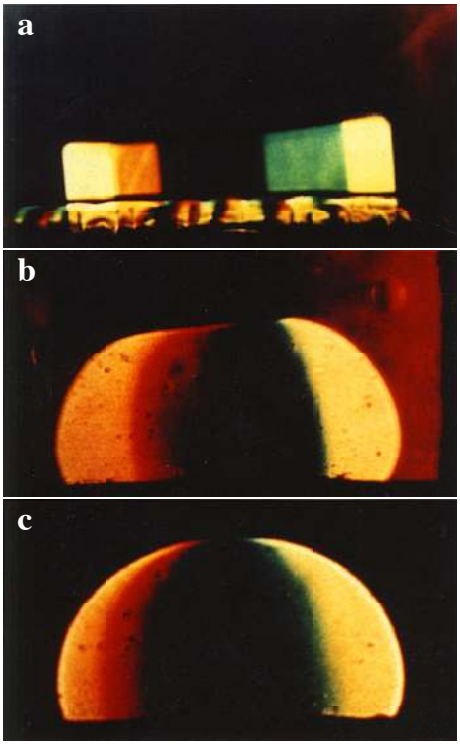

Fig. 2 (online colour at: www.ann-phys.org) ^{4}He-single crystal in equilibrium with its superfluid exhibiting surface roughening detected by vanishing facets. a) $T = 0.4$ K. b) $T = 1.1$ K. c) $T = 1.4$ K. From [2].

Most surfaces melt at temperatures beyond the roughening transition, but well below the bulk melting temperature. There is manifold evidence for this so-called surface melting, or surface initiated pre-melting. Far below their melting temperature, ice cubes are covered by a thin liquid water layer. When they are brought into contact they quickly freeze together since the liquid layer in the contact area is no longer surface but becomes bulk and therefore gets solid at lower temperature than the surface. Closely related to surface melting is the observation that undercooling a liquid is possible but overheating of solids is not.

Apart from surface diffusion and surface anharmonicity, all the other temperature induced effects shown in Fig. 1 are phase transitions. Phase transitions occur because different phases partition their free energy $F = U - TS$ between internal energy $U(T)$ and entropy $S(T)$ in different ways. In order to minimize F, the system changes phase at a critical temperature, T_c. Competing phases are commonly characterized by the order parameter, having a finite value in the low-T phase and vanishing in the high-T one. The behavior of the order parameter near T_c distinguishes two quite different phase transitions. For a first order phase transition, the free energies of both phases cross at T_c and the order parameter changes discontinuously. Close to T_c there is phase coexistence as well as nucleation and growth of one phase in the other. In a second order, or continuous, phase transition the order parameter varies smoothly; close to T_c it follows $(T - T_\mathrm{c})^\beta$ with β being the critical exponent. The competing phases become indistinguishable at T_c. Universality imposes β to depend only on the symmetry of the system, as well as on the dimensionality of the order parameter and of space. Therefore second order phase transitions at surfaces are expected to be different from those in bulk.

In what follows we highlight those aspects that do not depend on the details of the system but we also show specific examples in order to go into depth and to illustrate the differences between the systems. In order to make the paper lively, and to go beyond mere literature survey, we treat in each section questions of interest for the general reader. For instance, some surfaces such as NaCl(100), Pb(111), Al(111), Au(111) show no surface melting [3–5]. Why do they stay crytalline and solid until the bulk melting temperature is reached? Or how can one estimate the density of the adatom gas present at a given temperature for a given surface? This is of importance, not only for Ostwald ripening and mass transport, but also if other species are deposited they may condense the adatom gas into mixed structures. For organic molecules this leads to metal-organic structures without the need of metal deposition [6]. Where does a solid evaporate its atoms, do they go into the 3D gas phase from kink sites or from the 2D adatom gas? For readers wishing to go into depth we recommend at the end of this overview review articles or book chapters for further reading.

2 Surface diffusion

As the crystal temperature is raised starting from zero Kelvin, the first process getting activated is surface diffusion. This is the random walk of adatoms, molecules, small clusters, or vacancies over atomically flat terraces, or across atomic steps of a single crystal surface. Since this Volume deals with clean surfaces, we focus on surface self-diffusion, or homo-diffusion, where the diffusing species is of the same chemical nature as the substrate.

Surface diffusion establishes mass transfer along concentration gradients, but it also refers to the random walk of a constant concentration of diffusing species without any net flux of mass. The first case is called *mass transfer* and the second *intrinsic* diffusion [7]. For mass transfer diffusion, the concentration of random walkers n changes with temperature, location, and time, as particles are supplied from sources and consumed by sinks. The sources and sinks most often are kinks at atomic steps, but also screw dislocations, and even flat terraces where adatoms or vacancies can be created. The atomic processes associated with the sources and sinks, but also the mean square displacement between equivalent sites, are all thermally activated and therefore their respective rate is given by a Boltzmann term with an energy barrier and a pre-exponential factor. One defines the diffusion coefficient as the area traveled per time,

$$D = \frac{\nu_0 \lambda^2}{2d} \exp(\Delta S/\mathrm{k_B}) \exp(-\Delta H/\mathrm{k_B}T)\,, \tag{1}$$

with ΔS and ΔH being the entropy and enthalpy changes associated in the case of intrinsic diffusion D_I with hopping between equivalent sites, and in the case of mass transfer diffusion D_M in addition with the formation or annihilation of the adsorbed particle. λ refers to the jump length, ν_0 is called attempt frequency and is in the range of phonon frequencies of 10^{13} Hz, and d is the dimension which is 2, unless surface diffusion takes place along channels of a reconstructed surface where it is 1.

The temperature independent terms of Eq. (1) are often assembled into a common prefactor

$$D_0 = \frac{\nu_0 \lambda^2}{2d} \exp(\Delta S/\mathrm{k_B}). \tag{2}$$

For intrinsic diffusion, the entropy difference between the configuration in the minimum of the surface potential and the one in the transition state is negligible, $\Delta S = 0$. For typical values of $\lambda = 3$ Å and $\nu_0 = 10^{13}$ Hz this leads to the universal pre-exponential factor of $D_{0,\mathrm{I}} = 2 \times 10^{-7}$ m^2/s, which is found in the majority of intrinsic diffusion studies. The pre-exponential factor can be related to the curvatures of the potential energy surface in the binding and transition state. The expressions above are based on Transition State Theory (TST) [8] which rests on the assumptions that the atoms stay long enough in their adsorption wells to thermally equilibrate between two subsequent jumps and that recrossing of the barrier is negligible. These conditions are met if $\mathrm{k_B}T \ll E_\mathrm{m}$, which is generally the case. For intrinsic diffusion the enthalpy change is the binding energy difference between initial and transition state and often referred to as diffusion or migration barrier $\Delta H_\mathrm{I} = E_\mathrm{m}$. In the majority of cases atoms jump by one lattice site at a time. Long jumps have been observed [9–13], but remain the exception.

When individual displacements of atoms are traced, one reports the jump rate $\nu = \nu_0 \exp(-E_\mathrm{m}/\mathrm{k_B}T)$ which is related to the diffusion coefficient by $D = \nu\lambda^2/2d$. Figure 3 shows the example of Cu adatoms diffusing on a Cu(111) surface. Sequences of scanning tunneling microscopy (STM) images enable to trace the atomic positions as a function of time and temperature. For sufficiently low temperatures the probability of atoms making one jump forth and a second one back in-between two images is small, therefore the abundance of displacement events from image to image directly gives the jump rate. Figure 3b) shows that this rate displays perfect Arrhenius behavior, i.e., its logarithm is proportional to $1/T$, confirming the validity of TST. One infers from this figure $E_\mathrm{m} = 40 \pm 1$ meV and $\nu_0 = 1 \times 10^{12.0\pm0.5}$ Hz for Cu(111) self-diffusion [14].

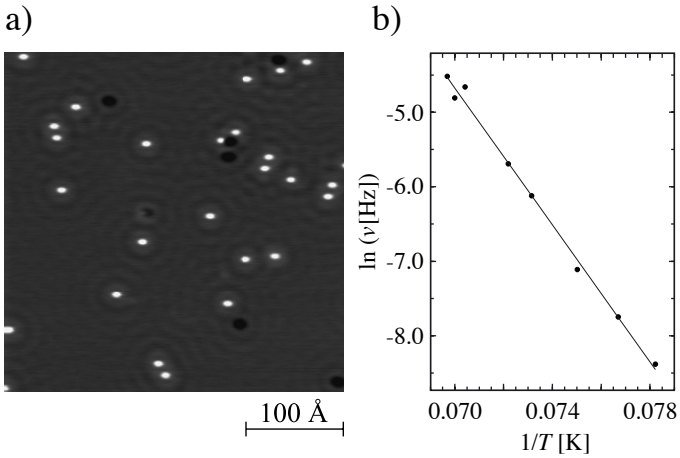

Fig. 3 Tracer diffusion of Cu adatoms on Cu(111) measured from time sequences of low-temperature STM images. a) STM image showing isolated Cu adatoms (coverage $\Theta = 1.4 \times 10^{-3}$ ML, 1 ML is defined by one adatom per substrate surface atom, tunnel voltage $V_\mathrm{t} = 100$ mV, tunnel current $I_\mathrm{t} = 0.5$ nA, $T = 13.5$ K, for time sequences see http://ipn2.epfl.ch/LNS/gallery/). b) Arrhenius plot of the jump rate of isolated Cu monomers. The STM tip had no influence on this rate for tunnel resistances $R_\mathrm{t} > 1 \times 10^8$ Ω. From [14].

In Fig. 1 we have placed the onset of surface diffusion at 10 % of T_m according to Cu/Cu(100). For that system the diffusion barrier is 0.36 ± 0.03 eV giving an onset temperature of 139 ± 12 K where $\nu = 1$ Hz ($T_\mathrm{m,Cu} = 1356$ K). For the close-packed (111) surface the barrier is one order of magnitude lower and

diffusion sets in at 15 ± 1 K, or 1 % of $T_{\rm m}$. While these values vary from element to element it is generally observed that close-packed surfaces have much lower diffusion barriers than the more open ones.

Note that observations such as the one shown in Fig. 3 are only possible if the adatoms are stable over a long time while they diffuse meaning that they do not disappear when coming close to each other or to steps. Therefore, even if the experiment reports on intrinsic diffusion, the absence of an effective sink is important. In our example the atoms are surrounded by concentric rings caused by Friedel oscillations in the underlying surface state. These charge density oscillations lead to weak oscillatory long-range interactions between the adatoms [14, 15]. For the present system they are accompanied by a short range repulsion of 12 ± 2 meV [16, 17] that prevents the atoms from forming clusters at the low temperatures used for this experiment. At higher temperatures the Cu adatoms form strongly bound dimers ($E_{\rm b} = 260$ meV [18]) or attach to steps.

Mass transfer and intrinsic diffusion can be linked by

$$D_{\rm M} = \frac{n}{n_{\rm sat}} D_{\rm I}\,, \tag{3}$$

where $n_{\rm sat}$ is the saturation value of the above introduced density of diffusing particles n. For self- or homo-diffusion the number of diffusing particles is generally strongly T-dependent due to adatom creation by evaporation from kinks onto terraces or by thermal adatom vacancy pair formation. Adatom creation from straight steps is found to be negligible [7]. At equilibrium one has

$$\begin{aligned}\frac{n}{n_{\rm sat}} &= \exp(-\Delta H_{\rm f,kink}/{\rm k_B}T)\exp(\Delta S_{\rm f,kink}/{\rm k_B}) \\ &\quad + \exp(-\Delta H_{\rm f,terrace}/{\rm k_B}T)\exp(\Delta S_{\rm f,terrace}/{\rm k_B})\,,\end{aligned} \tag{4}$$

where the index f refers to adatom formation. We note that sink terms can be included straightforwardly into this equation. One infers that $\Delta H_{\rm M} = \Delta H_{\rm I} + \Delta H_{\rm f}$ and $D_{0,\rm M} = D_{0,\rm I}\exp(\Delta S_{\rm f}//{\rm k_B})$. For systems with large adatom formation entropy one has $D_{0,\rm M} \gg D_{0,\rm I}$. If also the adatom formation enthalpy is large one has a crossover between intrinsic diffusion with constant particle density at low temperature to diffusion rates being dominated by particle creation at high temperature. For Si(100) self-diffusion this transition is situated well below the melting temperature [7].

For hetero-diffusion, all adsorbed particles can be mobile and one has $n = n_{\rm sat}$ and $D_{\rm M} = D_{\rm I}$. For a high density of mutually interacting particles one speaks of *collective*, *chemical*, or *Fickian* diffusion, the latter referring to Fick's law of diffusion that relates D to a concentration gradient [19]. In heterogeneous catalysis the surface concentrations of simultaneously diffusing species are large and the diffusion coefficient is strongly coverage dependent due to the interactions.

Alternatively to thermal activation, diffusion can occur by quantum mechanical tunneling. While the diffusion rate for D atoms on Cu(100) shows Arrhenius behavior down to lowest temperatures, H atoms diffuse for $T < 60$ K at a constant rate independent of temperature [20]. Above 60 K H atoms have exactly the same diffusion rate as D. Both species are chemically identical and have the same diffusion barrier which they cross by thermal activation. For H, being the lighter one of the two, tunneling opens up as new diffusion mechanism at low T. Since this process is not thermally activated H diffusion by tunneling is at very low temperature by orders of magnitude larger than the thermal one of D. However, diffusion by tunneling remains the exception and is restricted to very light adatoms and dominates the rates only at very low T.

The experimental methods used to measure surface diffusion are manifold and we restrict ourselves to a description of a few of the most relevant ones. Amongst the microscopy techniques, the field emission microscope (FEM) has been employed to monitor diffusion indirectly by the adatom density fluctuations it induces [19, 21, 22]. Such fluctuations in the probe region cause local work function changes, which are detected by fluctuations in the emission current. The potential of FEM to watch diffusion of individual atoms with ps time resolution by using a fast sweep of the field-emitted electron beam has also been

demonstrated [23]. The field ion microscope (FIM) has been used to trace individual displacements of isolated diffusing species [24–27]. During diffusion the field is turned off not to perturb the diffusion rate. For subsequent imaging the FIM tip is cooled in order to freeze in the state after thermal diffusion since under the high imaging fields the atoms would diffuse much faster than their intrinsic thermal diffusion rate. Due to the fields applied in the imaging process FIM is restricted to adsorbate/substrate combinations with high binding energy, such as refractory metals.

As shown above, also STM can be used to study tracer diffusion. This can be done by sequential images revealing the individual atomic displacements [14, 28–30], or by images where atoms jump between successive line-scans giving estimates on the residence time of the adsorbed species [31, 32], or by tracking the diffusion of one atom with the tip [33]. STM does not have the restrictions of FIM to systems with high cohesive energies. Nevertheless, care has to be taken to perform the observations under conditions where one can safely exclude the influence of the STM tip on the diffusion rate [28, 29]. However, careful studies can reveal even very small diffusion barriers without perturbation, see e.g. Fig. 3. Atoms can also be moved around using the tip-surface interaction [34]. The force necessary to push an atom over the barrier to its neighboring binding site has been measured with an atomic force microscope (AFM) [35]. From integrating this force over the distance one can infer the work needed to push the atom over the barrier, which was found for Co/Pt(111) to agree very well with formerly measured diffusion barriers. With this technique one can potentially also measure binding energy differences between different surface sites. The binding energy difference between initial and final site can be measured by pushing the atom in both directions and subtracting the two barriers. Diffusion can also be studied with the STM in looking at the flicker noise caused by atoms diffusing through tunnel junction [36, 37].

The energy of surface diffusion can further be inferred from quasi-elastic helium atom scattering (HAS) [38, 39]. The kinetic energy of the He atoms that are elastically scattered from diffusing atoms reveals a small additional broadening due to momentum transfer. In analogy to quasi-elastic neutron scattering, which has been used to study diffusion in solid and liquid bulk samples, this can be used to measure diffusion rates. Other than STM, this technique can be applied up to $T_{\rm m}$ [40].

Another way to learn about diffusion is to study the evolution of the surface morphology caused by mass transport diffusion. For instance, the disappearance of adatoms due to the onset of diffusion has been studied by low-energy ion scattering (LEIS) [41]. However, this usually reveals a threshold temperature where a certain diffusion rate is reached, and not the whole T-dependence needed for independent determination of ν_0 and $E_{\rm m}$. The decay of concentration profiles has been studied by scanning electron microscopy (SEM) [42], STM [32], and by photo-electron microscopy (PEEM) [43]. The island densities forming during sub-monolayer growth are related to tracer diffusion coefficients by nucleation theory [16, 44] and/or kinetic Monte-Carlo simulations [45]. Temperature and deposition flux dependent island densities have been reported by SEM [46] and variable-temperature (VT) STM [29, 45, 47–49] and interpreted in terms of diffusion parameters and cluster binding energies. Similarly, island separations have been measured by high-resolution low energy electron diffraction (HRLEED) [50–52], and step densities by HAS [53]. A useful concept for diffusion studies is the use of tracer atoms enabling to follow the diffusing species. The diffusion of the radioactive isotope ^{8}Li on Ru(0001) has been studied by coverage dependent spin lattice relaxation rates extracted from nuclear magnetic resonance (NMR) [54] and In atoms taking substitutional sites in Cu(100) have been used to see Cu vacancy diffusion [55]. The latter example will be discussed in more detail in the next section.

3 Two-dimensional adatom and vacancy gas

From the preceding section it is clear that heating up a surface leads to the creation of adatoms and/or vacancies. As stated above, adatom creation from straight steps is experimentally found to be negligible [7], therefore the only possible sources of adatoms are kinks and terraces. They appear with their corresponding entropy and energy terms in Eq. (4) which determines the adatom density. Adatom creation from terrace

sites generally has higher formation energy than kinks, however, the terrace sites from which an adatom can be created are much more abundant than kinks at steps. In an Arrhenius representation, the terrace source term therefore has a steeper slope but also a higher intercept at the origin (pre-exponential factor) and may thereby cross the more shallow slope and lower intercept line representing kinks as adatom source. This crossing is observed for Si(100) at 1025 K; below this temperature adatoms come from kinks above from terraces [7]. Vacancies can be created at straight steps or terraces, and a similar equation can be written down for their density.

Let us start by one example illustrating the role of a gas of surface vacancies. As briefly mentioned above, In tracer atoms that substitute Cu atoms in the first atomic plane of a Cu(100) surface have been used to follow self-diffusion [55,56]. The In atoms are discerned from Cu by their different apparent height such that their position can be traced in subsequent STM images. For such image sequences recorded at around room temperature this has led to two unusual observations. The In atoms jump over distances of up to 5 lattice spacings, and adjacent In atoms separated by a few atomic distances often jump simultaneously. The jump rate is with $\nu = 10^{-2}$ s much lower than the image acquisition rate, excluding the long jumps to be caused by a sequence of individual jumps over one lattice spacing in-between consecutive STM images. The interpretation has been that there is a low concentration of very rapidly diffusing vacancies. Each time the trajectory of the random walk of a vacancy approaches an In atom, it returns to this atom several times between subsequent STM images leading to the long jumps. In accordance with this idea, the jump length distribution has the shape of a modified Bessel function, and not the Gaussian shape expected for statistically independent jumps by single lattice sites. The vacancy also hits the neigboring In atoms explaining their strong tendency for simultaneous motion. The finding that homogeneously deposited In atoms penetrate the terraces from the steps has been interpreted as vacancy assisted diffusion, discarding the alternative interpretation of these findings as adatom assisted diffusion by exchange.

The mechanism of vacancy assisted diffusion of In is believed to function like a slide puzzle, where square tiles can be rearranged by moving a single missing tile through the puzzle. The vacancy formation energy has been calculated to $\Delta H_{\rm f} = 0.474$ eV [57] and the effective energy barrier for vacancy assisted diffusion has been determined to $E_{\rm m} = 0.72 \pm 0.03$ eV (with $D_0 = 10^{-9.5\pm0.2}$ m^2/s) [58]. Referring to the preceding section, the energy barrier of vacancy assisted mass transfer diffusion of In atoms is the sum of the source term, i.e., the vacancy formation energy and of the process by which the vacancy moves, which is the lateral exchange of a vacancy with the In atom. From the above energies, the barrier of the latter process is therefore estimated to 0.25 eV. With $\nu_0 = 10^{13}$ Hz this leads to a vacancy diffusion rate of $\nu = 10^9$ Hz at room temperature and explains the fact that the vacancies themselves are invisible to the STM. It is important to realize that the In atoms have only been necessary as markers, also the bare Cu(100) surface has at 300 K a dilute vacancy gas. One can estimate the density of this vacancy gas by means of Eq. (4). Using the calculated $\Delta H_{\rm f}$ value and ignoring entropy contributions one obtains $n = 10^{-8}$ ML at 300 K. Despite this low density, the diffusion of In, the one of Pd [57], and also Ostwald ripening of monolayer heigh Cu islands [59] are all dominated by the presence of vacancies on the Cu(100) surface! Whether mass transfer diffusion is dominated by vacancies or adatoms depends on the respective concentrations and diffusion barriers. For Cu/Cu(100), the latter have been calculated to 0.42 and 0.52 eV, respectively [60], such that vacancies are expected to dominate mass transfer at room temperature for adatom concentrations below 10^{-8} ML.

Estimates of the equilibrium adatom density at a given temperature can be derived from the adatom creation energies of the system of interest. These energies can of course be calculated, as the values above for vacancies. However, precise experimental values can be derived from thermal desorption spectroscopy (TDS), as will be illustrated for the example Ni/W(110) [61].

Nickel adsorption on a W(110) surface is entirely reversible. This means that there is no adsorption barrier and therefore the adatom binding energy $E_{\rm b}$ equals the adatom desorption energy $E_{\rm des}$ which can be measured by TDS. In addition, it implies that Ni does not form an alloy with W and therefore desorbs instead of diffusing into the bulk. Figure 4 shows $E_{\rm des}$ (left) and $\nu_{\rm des}$ (right) derived from a series of coverage dependent thermal desorption spectra [61]. For coverages below $\Theta = 0.4$ ML one finds two

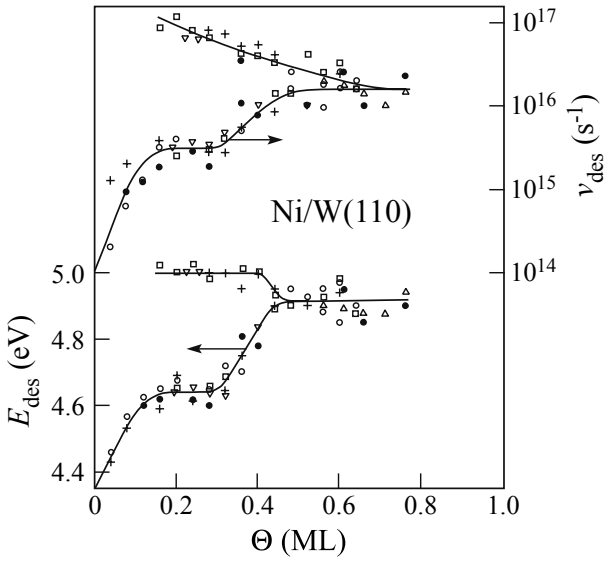

Fig. 4 Coverage dependent desorption energies and pre-exponential factors derived from TDS for Ni/W(110) [61]. The upper branches correspond to atoms directly evaporating from steps, and the lower ones are caused by atoms desorbing from a 2D adatom gas on the W(110) terraces.

branches of the desorption energy and of its attempt frequency. The respective upper branches are caused by direct desorption from kinks at steps, while the lower ones correspond to desorption from a 2D adatom gas on the atomic terraces. It is further evident from Fig. 4 that both parameters, $E_{\rm des}$ and $\nu_{\rm des}$ show a strong dependence on coverage, particularly for the lower branches. The initial linear increase of $E_{\rm des}$ with increasing Θ found for the lower branch is indicative of attractive adsorbate-adsorbate interactions in the adatom gas. The following shoulder is interpreted as being due to desorption from a dimer gas giving access to the dimer bond energy on this surface. The data points at low coverage are sufficiently numerous that extrapolation to the zero coverage limit of single non-interacting adsorbed adatoms is possible. For our example one derives adatom terrace and kink binding energies of $E_{\rm b,terrace} = 4.36 \pm 0.03$ eV and $E_{\rm b,kink} = 4.95 \pm 0.05$ eV, repspectively. The adatom formation energy is the difference between the two and amounts to $\Delta H_{\rm f} = 0.59 \pm 0.06$ eV. From this we derive the density of Ni adatoms on a sub-monolayer Ni covered W(110) surface to be $n = 10^{-10}$ ML at room temperature and $n = 10^{-5}$ ML at 600 K.

A rough estimate of $\Delta H_{\rm f}$ can be obtained for homo-systems by comparing the vaporization energy with the cohesive one [62]. The latter corresponds by definition to the binding energy of an atom at a kink site. If there is a difference between the two, desorption from terrace sites competes with direct desorption from kinks, and the energy difference can be associated with $\Delta H_{\rm f}$. For Cu one finds $E_{\rm coh} - E_{\rm vap} = 3.49$ eV $- 3.16$ eV $= 0.33$ eV [63]. Unfortunately, this is not a value for a specific surface orientation. However, assuming it to be a reasonable approximation for Cu/Cu(100) leads to an estimate of $n \approx 3 \times 10^{-6}$ ML adatoms at 300 K. It must be emphasized that these are rough estimates since they do not consider entropy and ignore the surface orientation. A possible sink for the adatoms is their condensation into small clusters. However, the binding energy of an adatom to the edge of such a cluster is usually smaller than to the kink between two straight step sections and therefore cluster formation is reversible. If organic molecules are evaporated onto a Cu(100) surface held at room temperature the Cu adatoms are incorporated into metal-organic networks [6]. These networks need higher Cu densities than the value estimated above, however, as long as steps are not passivated by the molecules there is a constant adatom supply from kinks until the metal-organic network covers the entire terraces.

To finish this section we cite two further examples where adatom, respectively, vacancy creation have been observed. A combined inverse photo electron spectroscopy (IPES) and ion scattering study performed on Cu(110) reported intensities decaying for $T > 450$ K much stronger than expected from the lattice vibrations [64]. The strong decay of the ion scattering intensity was only found for the $\{1\bar{1}0\}$-directions. From incident angle resolved ion scattering intensities it is suggested that the surface atoms are from 450 K

on displaced sufficiently far from their lattice sites to give access for the incident ions to the next nearest neighbor atoms in the first atomic plane, which are otherwise blocked. The large displacement is due to higher vibration amplitudes of the atoms in the first atomic plane and will be treated in the following Section. However, there is a second deviation in the ion scattering data from the expected one, namely there is too much intensity at small angles. This can only be reconciled by an adatom gas scattering the ions back at small angles since they are not screened by neighbors. The concentration of the adatom gas showed Arrhenius behavior and led to $\Delta H_{\mathrm{f}} = 0.2 \pm 0.1$ eV in good agreement with 0.27 eV inferred by Gorse [65]. The interpretation of an adatom gas is corroborated by the non-linear decay of the logarithm of the IPES intensity which can only be reproduced by adding a defect term to the Debye-Waller factor accounting for bulk lattice vibrations. The IPES decay is caused by scattering of the incident electron wave by the adatoms (defects) and the vibrating surface atoms. Perfect fits to the IPES intensity are obtained with the defect creation energies given above. The strong directional dependence of the ion intensity decay can be due to strongly anisotropic surface diffusion of the adatom gas, which is indeed expected for the atomic channels present on fcc(110) surfaces.

The Ge(111) surface has been reported to undergo a reversible disordering transition at 1050 K [66]. This temperature is 160 K below the bulk melting temperature and therefore in a regime where surface roughening or melting are the expected phase transitions, see Fig. 1. These transitions could clearly be ruled out, however. The low energy electron diffraction (LEED) spot intensity $I(E)$-and $I(T)$-curves showed the crystalline order between the atomic (111) layers to be preserved up to, but possibly not including the uppermost double-layer. This rules out surface melting. Surface roughening has been ruled out based on angular peak profiles. The authors proposed a domain disordering mechanism, but also noted that it does not explain all their observations. A slightly different interpretation has been derived from electron energy loss spectroscopy (EELS) [67]. This technique reveals the structure transition by its effect on the electron density of states (DOS). The $3d$-Ge core level threshold is far less structured for amorphous than for crystalline Ge, while liquid Ge is a metal with a flat DOS and therefore shows sharp step-like Ge-$3d$ loss features. From comparison with these known loss features, the authors concluded the high-T Ge surface to be an amorphous layer. More light has been shed onto this transition from gracing incident X-ray scattering (GIXS) experiments [68]. The bulk forbidden (10) and (20) peaks remained sharp ruling out thermally generated steps and therefore surface roughening and melting in accordance with LEED and EELS. With increasing temperature, the integrated peak-heights of these two peaks decreased significantly steeper than the one of the (11) peak, which showed perfect Debye-Waller decay. After this steep decrease the intensity reached a minimum at 1150 K from where on it increased again. The decrease can be explained by the proliferation of adatoms or vacancies, however, the minimum and the foll wing partial intensity recovery can only be explained by vacancies in the first bilayer [68].

4 Surface phonons and anharmonicity

The atomic interaction potentials in solids are anharmonic. Generally, stretching a bond is easier than its compression, i.e., the potential is steeper when going from its minimum to smaller than to larger distances. This asymmetry leads to thermal expansion and to the monotonic increase of the lattice heat capacity beyond the constant value predicted by the law of Dulong and Petit. The reduced coordination of the surface atoms, and the boundary condition of vanishing forces at the cleavage plane, give the surface its characteristic phonon dispersion relation, anharmonicity, and thermal expansion. We describe how surface phonons are experimentally observed and then concentrate on surface anharmonicity.

Historically, EELS using primary electron energies in the range of 5 eV was the first technique to detect surface phonons. The long wavelength optical surface phonons were the first to be detected due to their relatively high energy. Examples are the energy loss and gain of 69 meV by the creation, respectively, absorption of a surface phonon by the electrons interacting with ZnO(1100) [69], or similar gain and loss

peaks appearing at 56 meV for Si(111)–(7×7) [70]. Increasing the energy resolution of this technique to $\Delta E = 1.0$ meV enabled to map out the entire dispersion relation of surface phonons.

Low energy electrons interact with many atomic layers and therefore report on surface and bulk properties. Inelastic He atom scattering (HAS) is intrinsically surface sensitive and has time-of-flight energy resolution of $\Delta E/E = 1$–2 % at incident energies of 10–100 meV, making it an ideal probe for surface phonons. Early applications of this technique were the collective surface vibrations of NaF(100) [71], Si(100)–(2×1) [72], and Pt(111) [73].

Surface anharmonicity manifests itself, e.g., by surface interlayer distances varying with temperature in a different way than the ones in bulk. At low temperature, the uppermost atomic plane of Pb(110) is relaxed inwards by 17 % of the bulk layer spacing in order to compensate for the missing bonds of the surface atoms. When approaching 500 K this inward relaxation shrinks to only 5 %, see Fig. 5. Thus the thermal expansion of the surface layer spacing is significantly above the bulk expansion which would result in the horizontal dash-dotted line.

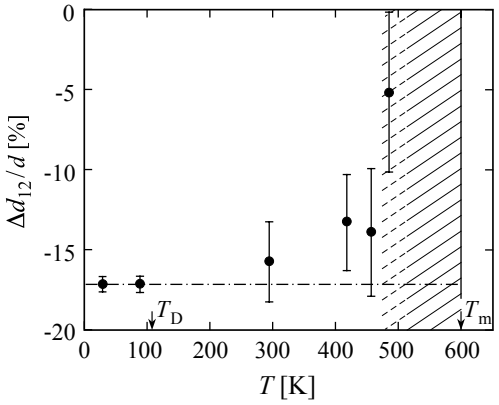

Fig. 5 Surface layer spacing normalized to bulk layer spacing versus temperature for Pb(110). The temperature regime where surface melting occurs is hatched. The dashed part of the hatched region marks temperatures where the surface region contains an adatom gas with a coverage of $0.1 \leq \theta \leq 0.5$ ML [74].

A second manifestation of surface anharmonicity is the temperature dependent peak intensity and peak profile of backscattered probe particles. For a harmonic bulk crystal one expects that the mean square vibrational amplitudes of the atoms increase linearly with T, and that the scattering intensity decays exponentially with T, as expressed by the Debye-Waller factor. Bulk anharmonicity leads to deviations from this behavior. Surface anharmonicity is generally larger, see Fig. 5, and therefore it can be recognized by larger deviations from a harmonic crystal than the ones expected from bulk anharmonicity. The part coming from surface anharmonicity can further be distinguished from the bulk part by comparing surface with bulk sensitive scattering geometries and/or techniques. Several surface sensitive scattering techniques showed for Cu(110) at temperatures beyond 550 K drastic deviations from the behavior expected for a harmonic crystal. One example is the specular reflectivity in HAS, which follows the expected Debye-Waller decay until 550 K and then decreases much more strongly, see Fig. 6a) [65, 75]. This has been attributed to strongly enhanced effective mean square displacements due to large surface anharmonicity for that system [75]. Medium energy Ion scattering (MEIS) and impact collision ion scattering spectroscopy (ICISS) confirmed this interpretation [64]. As seen in Fig. 6b), the mean-square vibrational amplitudes obtained from the various techniques are in very good agreement with each other and all show the high temperature deviation from the linear behavior expected from harmonic potentials and drawn as full line.

X-ray scattering data obtained on Cu(110) have initially been interpreted in terms of surface roughening [77]. Since all other scattering experiments on this surface were reminiscent of surface anharmonicity, it is very likely that also the X-ray data can be reconciled this way. Instead of proving this we give one criterium clearly excluding a roughening transition of this surface. Surface roughening will be discussed in more detail below. However, we note already here that statistical mechanics predicts surface roughening to give rise to the following very specific peak profiles of elastically scattered He atoms [78, 79]. The intensity in the wings of the diffraction peaks is predicted to decay with increasing parallel momentum change $\Delta k_{||}$

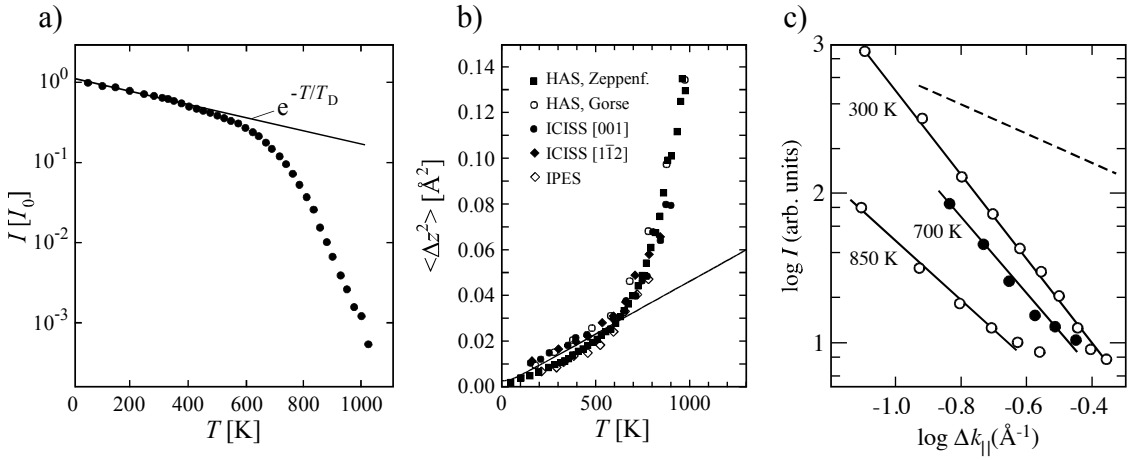

Fig. 6 a) Normalized specular He reflectivity on Cu(110) deviates from Debye-Waller decay for $T \geq 550$ K ($E = 18.3$ meV, $\Theta_i = \Theta_f = 45°$) [75]. b) Effective mean-square vibrational amplitudes of the Cu(110) surface atoms inferred from HAS [65, 75], ICISS, and IPES [64]. c) He specular peak profiles measured on Cu(110) ($E = 18.3$ meV along [001] azimuth) [75, 76].

according to a power law for a given temperature and with an exponent decreasing with increasing T. The roughening temperature is reached when this exponent takes on the value -1. While this prediction has been confirmed experimentally for surfaces showing roughening transitions, such as Ni(113) [76], the peak profile analysis of Cu(110) does not exhibit the characteristic features of roughening. As seen in Fig. 6c) the exponents are smaller than -1 (dashed line) for all temperatures and they vary only slightly from -2.8 at 300 K to -2.0 at 880 K. This clearly rules out surface roughening of Cu(110). All experimental observations on this surface are consistently described by its large anharmonicity.

A quantitative idea of the difference between bulk and surface anharmonicity of this system can be gained from a HREELS study reporting 4.5 times higher surface anharmonicity for vibrational motion normal to the surface than for similar motion in bulk [80]. The higher anharmonicity entails significantly softer modes leading to higher vibrational amplitudes and significantly smaller Debye temperatures for surface than for bulk. For our example of Cu(110) these are $T_D = 343$ K for bulk vs. $T_{D,surface} = 150 \pm 20$ K for the collective vibrations at the surface [64]. Anharmonic effects become apparent for Cu(110) at 550 K which is 41 % of the bulk melting temperature, see Fig. 1.

The anharmonicity of a surface depends on its crystallographic orientation. Figure 7 compares the temperature dependent effective mean square displacements of Cu(110) and Cu(100) [76]. At low temperature both surfaces show the linear increase expected from a harmonic potential, then they both exhibit a much larger increase due to surface anharmonicity. The deviation from the linear increase is situated at about 300 K lower temperature for the (110) than for the (100) orientation. This is likely due to a stronger anharmonicity on the (110) face than on the (100) face. In accordance with this assignment one finds that the temperature dependent relaxations of interlayer distances are much stronger for the (110)-oriented faces than for other low-index surfaces of lead.

In summary, the interaction potentials at surfaces are often more anharmonic than the ones in bulk and this effect is more pronounced for the more open surfaces presenting lower-coordinated atoms. Quite general, the different depth and curvature of the potential of surface compared with bulk bonds is expected to be most relevant to the thermodynamic properties of nanostructures, where surface bonds represent a significant fraction of the overall binding energy. In accordance, the heat capacity of nanostructures significantly deviates from bulk values, for low temperatures up to above the Einstein temperature, due to surface phonons and due to the fact that boundary conditions imply for a particle diameter d a minimum normal mode vector $k_{min} = \pi/d$ [82].

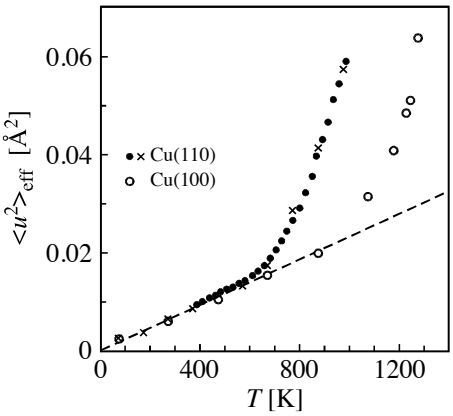

Fig. 7 Temperature dependent mean-square vibrational amplitudes of surface atoms inferred from HAS for two low-index surfaces of Cu. The linear increase expected from harmonic potentials is shown as dashed line. The data for Cu(100) (○ [81]) deviate at much higher T from this line than the ones for Cu(110) (x [65], • [75]).

5 Thermal surface reconstructions

Clean surfaces often rearrange their atoms in the first atomic plane in order to increase their coordination and or density. To take place, these surface reconstructions may require a certain temperature. One distinguishes two cases. In the first the surface reconstruction appearing above the transition temperature remains stable all the way down to low temperature, whereas in the second there is a reversible first order phase transition between two surface terminations. In the first case the surface needs to overcome an activation barrier to get out of its metastable state and achieve the reconstruction, which is the thermodynamic ground state down to low T. The thermal evolution is dominated by kinetic barriers but not by minimization of the surface free energy. In the second case the higher temperature phase is a thermal surface reconstruction, which appears when the surface is annealed beyond the transition temperature and disappears once it is cooled below. We discuss one example for the first case of an irreversible transition and two for the second case of thermal surface reconstructions which represent true phase transitions.

The bulk terminated (1×1) Ir(100) surface is metastable and transforms irreversibly into a (1×5) phase at 800 K [83]. The first atomic plane of the (1×5) phase is hexagonally close-packed increasing the atomic surface density by 20 % and the lateral coordination from 4 to 6 with respect to the more open square substrate lattice. This reduces the surface tension, which is particularly large for Ir, having one of the highest surface tensions among the elements. It countervails the energy cost due to the misfit between the topmost hexagonal surface and the underlying square substrate. The temperature and time dependent growth of the (1×5) phase could be followed by LEED giving access to the energy barrier of 0.9 eV/atom separating the two structures [83].

The first example of a true first order phase transition is Si(111). At moderate temperatures, this surface has a (7×7) reconstruction described by the Dimer-Adatom-Stacking fault (DAS) model, which was first proposed based on transmission electron microscopy (TEM) observations [84]. The real-space confirmation of this model was one of the first successful applications of scanning tunneling microscopy (STM) [85]. Refinement of the structure, identifying the precise atomic positions, has been achieved by diffraction techniques [86–89]. Due to the complexity of this structure, it has also been a test case of numerous high-resolution AFM studies [90–93]. Heating this surface above $T_c = 1200$ K causes a transition to a (1×1) phase [94]. Upon cooling slightly below T_c nuclei of the (7×7) phase reappear and already 30 K below T_c this phase covers again the entire surface [95]. The coexistence of both phases is characteristic of a first order phase transition which is expected from symmetry considerations for that system [96].

The Pt(111) surface is unreconstructed at moderate temperatures and reconstructs reversibly at 1330 K into an isotropically compressed surface layer [97, 98]. The bulk terminated surface is under tensile stress, but incorporation of extra atoms takes only place when these atoms are present as adatom gas on the terraces, which requires the high temperature. When they have to be taken from steps their chemical potential is too high to be overcome below 1330 K, and the surface remains unreconstructed. This view is supported

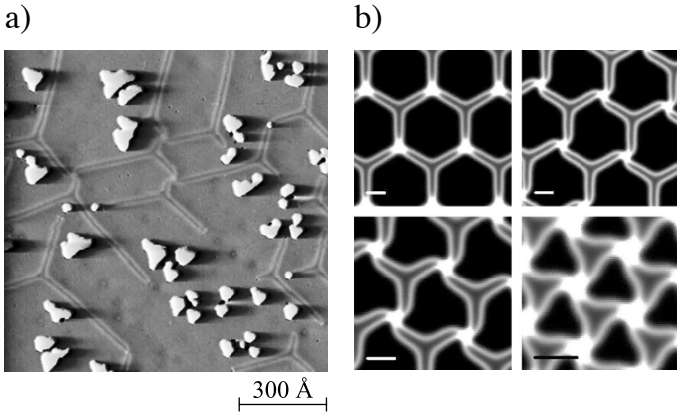

Fig. 8 Pt(111) surface reconstruction induced by Pt adatom gas. a) STM image of a Pt(111) terrace with bright double reconstruction lines and monolayer high Pt islands. In order to nucleate the reconstruction, the surface has been irradiated by 5 keV Xe^+-ions at 300 K (dose 1.3×10^{-4} ML). Subsequent deposition of 0.08 ML Pt at 300 K led to the formation of the characteristic elements of the reconstruction network (figure kindly provided by T. Michely, see also [100]). b) Structures for different atomic densities in the first layer of Pt(111) obtained from a 2D Frenkel-Kontorova model with parameters from *ab-initio* calculations (bars are 50 Å, figure kindly provided by R. Pushpa and S. Narasimhan, see also [101]).

by the fact that the surface reconstructs already at $T = 400$ K when extra Pt adatoms are deposited [99], and already at $T = 300$ K when reconstruction nuclei are created by ion bombardment with a low fluence [100].

The structure of the Pt(111) reconstruction is very similar to the Au(111)–$(\sqrt{3} \times 22)$ reconstruction [102]. Due the increased atomic density, the first atomic plane has partial surface dislocations which appear bright in Fig. 8 and separate fcc from hcp stacking areas. The dislocations allow to introduce half an atom per atomic dense-packed row. The partial dislocations arrange into pairs, which limits the faulted hcp areas to narrow stripes between the dislocation pair, while the majority of the surface remains in the energetically favored unfaulted fcc stacking. In contrast to Au(111), the dislocation pairs on Pt(111) are arranged in a network [103]. The characteristic elements of the network are stars where three dislocation pairs meet. As seen in Fig. 8a) there are stars with a dark center where the dislocations enter straight, and stars with a bright center where the dislocations curl either left or right. These features are reproduced in a 2D Frenkel-Kontorova model using input parameters determined from *ab-initio*-calculations for Pt(111). Figure 8b) on the upper right shows the structure with 2.9 % increased surface density and optimized angle between first and subsequent planes showing the experimentally observed [99] alternations of dark-straight and bright-curled stars [101]. The fact that extra adatoms induce the surface reconstruction has the side effect to induce the most perfect layer-by-layer growth for Pt/Pt(111) [104]. This is caused by two very different adatom mobilities on islands and terraces [105]. The Islands are unreconstructed and therefore adatoms diffuse very fast, while the diffusion on the terrace is slowed down by the reconstruction [106]. This gives the atoms on-top the islands many attempts to descend the steps at the island edges leading to 2D growth.

The thermal surface reconstructions of Si(111) and Pt(111) take place at similar transition temperatures, when these are scaled to the bulk melting temperature, $T_c/T_m(\mathrm{Si}) = 1200\,\mathrm{K}/1683\,\mathrm{K} = 71$ %, vs. $T_c/T_m(\mathrm{Pt}) = 1330\,\mathrm{K}/2045\,\mathrm{K} = 65$ %. The latter value has been used to situate this phase transition in Fig. 1.

6 Surface roughening

Surface roughening [107, 108] is the spontaneous creation of atomic steps rounding the sharp edges between the low Miller index faces by which a crystal is bound at low temperature. It is related to the anisotropy of the surface tension γ and to its temperature dependence. At temperatures far below the roughening transition γ has cusp shaped minima which are sharpest and deepest for the low-index faces. The angular dependence of γ can be inferred via the Wulff theorem [109] from the shape of single crystals when they are in equilibrium with their vapor. Establishing this equilibrium under clean ultra-high vacuum (UHV) conditions is difficult for elements with high vapor pressure. Au crystallites had to be heated inside a closed box with walls made from Mo to which Au does not condense at the applied temperatures [110]. Without this box, the surrounding vapor pressure would have been too low and the crystal would have sublimated before reaching its equilibrium shape.

For the metals Pb, Sn, and In, the vapor pressure is very low, even at the bulk melting temperature. Evaporation is therefore negligible and equilibrium shapes can be reached to a very good approximation under UHV conditions. Figure 9a) shows a UHV-SEM image of a lead crystal on graphite displaying a number of low index facets [111]. The polar plot of the surface tension inferred from the relative facet sizes is shown in Fig. 9b). It exhibits a sharp cusp at $\{111\}$ and a less sharp one at $\{100\}$. Both become flattened out with rising temperature as the anisotropy of γ gets reduced.

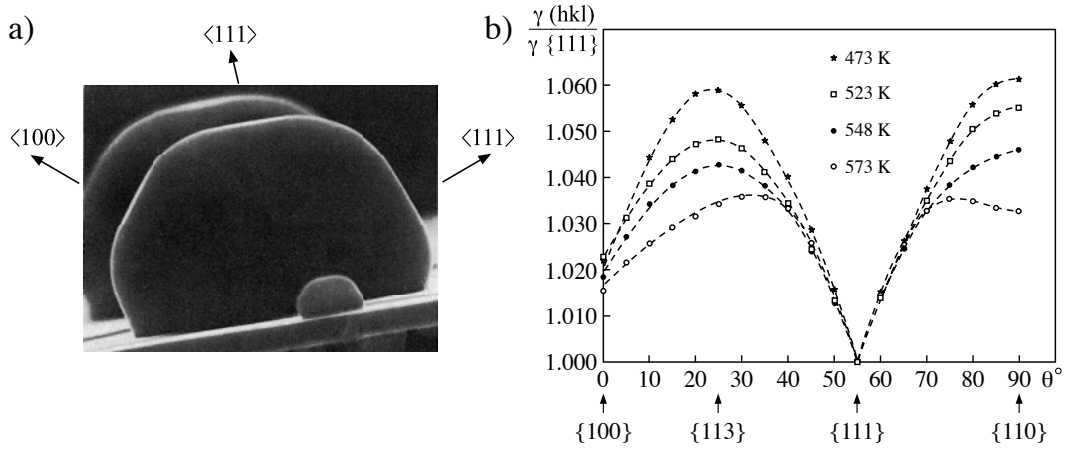

Fig. 9 a) UHV SEM image of a lead crystal at 473 K. b) Anisotropy of the surface tension as function of temperature [111].

The slope of γ at a cusp is proportional to the step free energy β, since orienting the surface by some angle away from the cusp requires creation of a proportional amount of monatomic steps. Burton, Cabrera, and Frank predicted the step free energy to vanish well below the bulk meting temperature [107]. The cusp is therefore predicted to disappear and the anisotropy of $\gamma(\theta, T)$ to vanish. A crystal initially bound by large low-index faces is expected to become a perfect sphere at the roughening temperature $T_{\rm r}$. Figure 10 shows that this is indeed what happens.

Roughening temperatures are different for different surface orientations, as expected from $k_{\rm B}T_{\rm r} \propto a^2\gamma$, where a is the in-plane lattice constant. One example where this difference appears is hcp ^{4}He coexisting with its own superfluid, see Fig. 2. Optical holographic interferograms revealed for that system $T_{\rm r}(1120) = 0.85$ K, whereas $T_{\rm r}(0001) = 1.08$ K [1]. As a consequence the (1120) face entirely disappeared at already 0.9 K, while the basal plane remained until close to its roughening temperature. $T_{\rm r}(0001)$ is with $T_{\rm r} = 0.94/T_{\rm m}$ very close to the bulk melting temperature of 1.15 K.

On fcc(110) surfaces of metals typical relative roughening temperatures are situated around $T_{\rm r} = 0.7/T_{\rm m}$, see Table 1. An exception is Pt(110)–(1×2), where monatomic steps are spontaneously formed

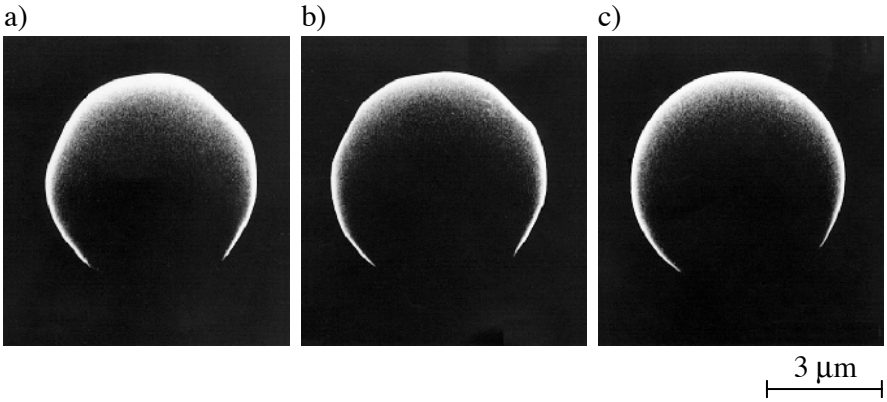

Fig. 10 Roughening transition for Pb-single crystals lying on graphite surfaces as seen by UHV SEM [111]. a) $T = 548$ K. b) $T = 599$ K. c) $T = 600$ K.

already at $T_{\rm r} = 0.53/T_{\rm m}$ [112]. One expects higher relative $T_{\rm r}$ values for the closer packed fcc(111) and fcc(100) surfaces. As discussed in Sect. 5, the (100) surface of some metals thermally reconstructs into a close packed monolayer residing on the square lattice of the subsequent layers. For Au(100) there is first a rotated corrugated hexagonal phase, taken on at 300–970 K, followed by a corrugated hexagonal phase, which gets disordered at $T_{\rm r} = 1170$ K [113–116]. This is with 87 % of $/T_{\rm m}$ significantly higher than the (110)-values in Table 1. The other extreme is the roughening temperature of Xe layers on a vicinal Pd surface, which has been determined to 68 K by photo-electron spectroscopy (PES) [117], whereas theoretical estimates for (111) planes where 138 K [107]. With the bulk melting temperature of 161 K one obtains $T_{\rm r} = 0.44/T_{\rm m}$, which is comparably low. However, due to interaction with the substrate thin film surfaces of Xe are expected to have different values than bulk Xe surfaces. Recent experiments on Pb layers on a Cu(111) surface show layer dependent roughening temperatures [118]. For this system, electron confinement between the vacuum/Pb and Pb/Cu interfaces gives rise to stable and unstable layer thicknesses [119]. This can be interpreted as layer-dependent surface tensions rationalizing the observed layer-dependent roughening temperatures.

Table 1 The roughening temperatures of some fcc(110)–(1×1) metal surfaces.

Surface	$T_{\rm r}$ [K]	$T_{\rm r}/T_{\rm m}$	References	$T_{\rm m}$ [K]
In(110)	290	0.69	[110]	429.8
Pb(110)	420	0.70	[110]	601
Ag(110)	790 ± 20	0.64	[120]	1234
Ni(110)	1300	0.76	[110]	1726
Cu(110)	1070	0.79	[112]	1356
Pt(110)–(1×2)	1080 ± 50	0.53	[121]	2041

Roughening transitions on vicinal surfaces appear at lower temperatures than on low-index surfaces [78, 79, 122–128] and manifest themselves by meandering steps due to the proliferation of kinks. The roughening of nominally stepped surfaces can be seen as roughening of low Miller index surfaces in one dimension less. In analogy with the vanishing step formation energy β, now the kink formation energy goes asymptotically to zero at the step roughening temperature [129].

7 Surface melting

Melting is a first order phase transition. As a consequence, the free energies of solid and liquid phase cross at $T_{\rm m}$, the order parameter changes discontinuously at this temperature, and phase coexistence, as well as nucleation and growth are expected. Since superheating of a solid above its melting point is not observed [130], however, nucleation barriers must be absent for ascending temperature, whereas they are present for descending temperature, since undercooling of liquids is possible. For instance, undercooling of water leads to the sudden nucleation of beautiful fractal ice crystals [131]. Melting is thus a reversible phase transition with kinetic barriers in one direction but not in the other. This miracle has to do with the surface.

In 1910 Lindemann made the observation that a solid melts when the vibration amplitude of its atoms reaches a critical fraction, of about 14 %, of the nearest neighbor distance in the bulk crystal lattice [132]. As we have seen above, surface atoms often have higher vibration amplitudes than bulk atoms due to surface anharmonicity. Consequently, Lindemann's melting condition is met earlier at the surface than in the bulk. This is called surface melting [5, 133]. As a consequence, when approaching $T_{\rm m}$ from below, the solid is covered by a thin layer of liquid acting as vast germ for bulk melting explaining why there is no barrier and why superheating is precluded. The existence of this layer can be suppressed by covering the surface with a material of higher melting temperature. This allows overheating, as nicely demonstrated for Ag ($T_{\rm m} = 1233$ K) crystallites covered with Au ($T_{\rm m} = 1336$ K) [134].

The first indirect observation of surface melting comes from Faraday who realized that ice at around 0°C is entirely covered by a water layer. As mentioned in the introduction, once two ice blocks are brought into contact, and kept thermally isolated from the environment, the water in the contact region quickly solidifies since it is not any more at the surface and the blocks freeze together.

The first direct experimental evidence of surface melting as an order-disorder transition of the atomic positions came from MEIS on a Pb(110) surface [135]. Figure 11 shows how this technique explores the number of disordered, molten atomic layers. MEIS typically uses proton beams with 100 keV kinetic energy. In order to detect surface melting, the incident beam is aligned along atomic columns of the bulk lattice such that the uppermost atoms shadow the deeper lying ones leading to a shadow cone. In addition, the detector is aligned in such a way that a blocking cone for the outgoing protons is formed, see Fig 11a).

Due to thermal excitation the atoms vibrate around their equilibrium positions which slightly reduces shadowing and blocking. Therefore some of the protons hit lower lying atoms, from which they get back-reflected with less kinetic energy due their energy loss along their path in the solid. This loss is called stopping power and amounts typically to 14 eV per Å path length [136]. At temperatures where the atoms

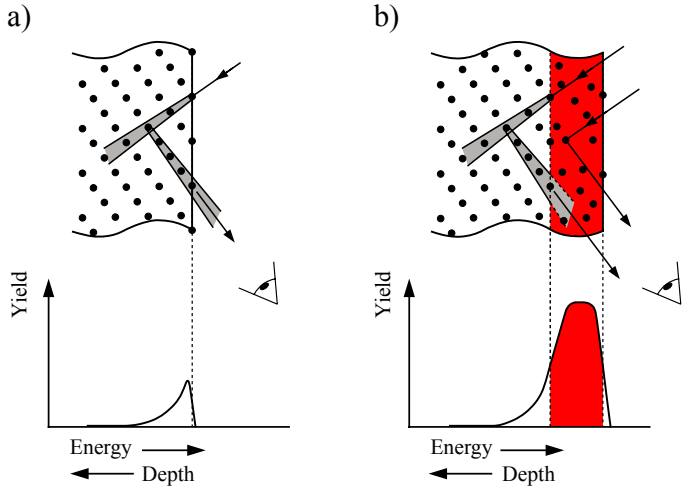

Fig. 11 (online colour at: www.ann-phys.org) MEIS under shadowing-blocking geometry. a) On a a well-ordered crystal surface the backscattered surface peak is small while b) a large additional backscattered signal is obtained from a crystal with a disordered surface layer on top. From [135].

are well localized around their equilibrium position, this leads to a large peak of protons with kinetic energy corresponding to back-relfection from the first atomic layer, followed by a steeply decreasing low energy tail, stemming from the few events where protons hit non-shadowed lower lying atoms and escape from there along non-blcoked trajectories, see Fig. 11a). When the surface is covered by a liquid film, the atoms in this film contribute almost fully to the high energy surface peak which increases its height, as can be seen schematically in Fig. 11b). At the same time, inelastic losses within the layer lead to a width of this peak which is related to the thickness of the liquid layer. Very much as in the low temperature case, this peak is followed by the low energy tail created by the solid buried by the liquid. As we will see below, height and width of the peak can be used to infer the number of molten layers.

Figure 12 shows MEIS data recorded on Pb(110) [137] and Pb(111) [138]. The temperature dependence of the peak height and width strongly depends on the surface orientation [139]. Whereas for Pb(110) the peak increases in height and becomes wide 20 K below $T_{\rm m}$, it remains almost constant up to $T_{\rm m}$ for Pb(111). The qualitative conclusion from the raw MEIS spectra is that the first surface pre-melts while the second does not.

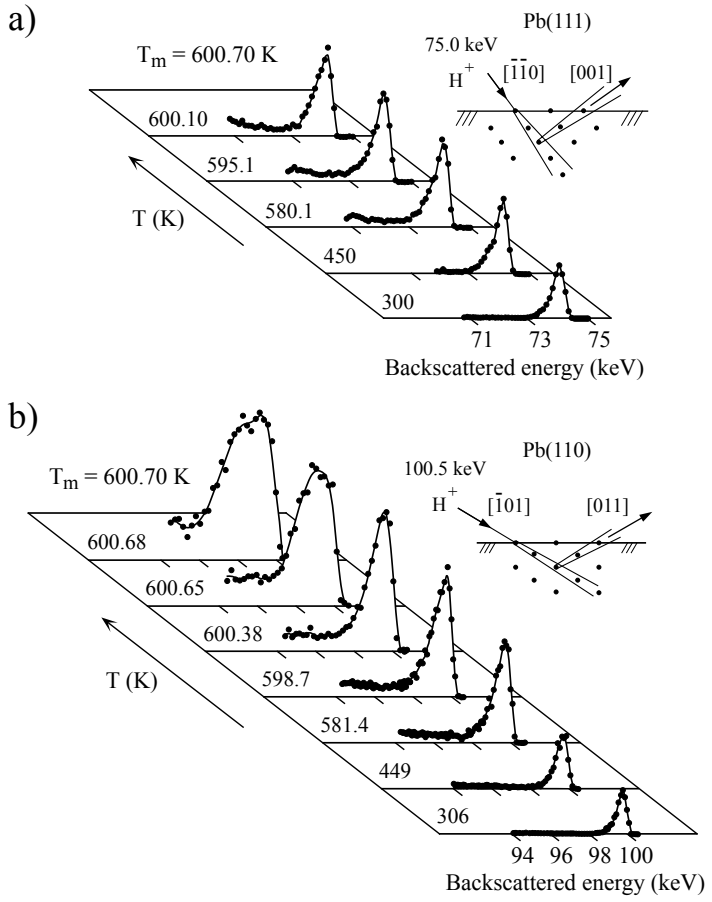

Fig. 12 Energy spectra of backscattered protons for increasing temperature, from a) Pb(111) and b) Pb(110). The insets show the shadowing/blocking geometry in which these spectra were taken. From [137, 138].

With the help of Monte-Carlo simulations the surface peak area can be associated with the number of molten atomic layers. Figure 13 shows the result for both surfaces. The curve expected from bulk lattice vibrations and bulk interlayer distances is denoted I in Fig. 13b) and lies below the data. Curve II accounts in addition for the enhanced surface vibration amplitudes and the relaxation of the first two interlayer distances, both are manifestations of surface anharmonicity as we have seen above. This curve describes the low-T data quite well. From 500 K on the number of visible layers is significantly enhanced compared

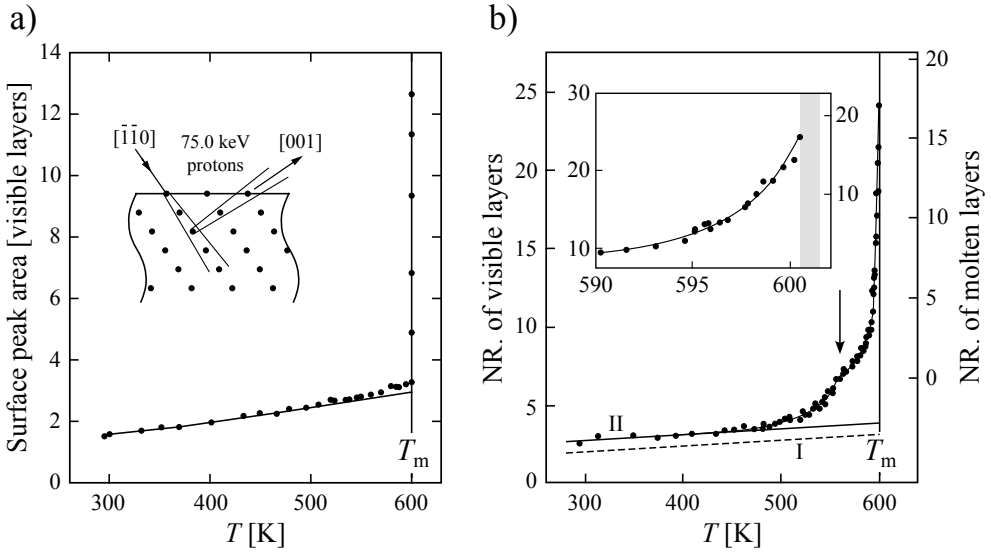

Fig. 13 The surface peak area for Pb(111), expressed as the number of visible monolayers, as a function of temperature for Pb(111) a) [139] and Pb(110) b) [135]. The experimental conditions for a) are given in its inset and the ones for b) in Fig. 12b). The solid curves are the number of visible monolayers calculated by Monte Carlo for a well-ordered thermally vibrating crystal. Curve I in b) shows the expected behavior from bulk vibrations and bulk interlayer distances while curve II adds surface anharmonicity. The arrow indicates the surface melting temperature. The curve in a) assumes 15 % enhanced surface vibration amplitudes but leaves the interlayer distances at their bulk values. The inset in b) enlarges the high-T region and shows the uncertainty on $T_{\rm m}$ as shaded area.

with the expectation from a well ordered vibrating crystal. The only way this could be reconciled in the Monte-Carlo simulations was to include molten layers on the vibrating solid. It is seen that the surface has up to 15 such layers at $T_{\rm m}$. The surface melting temperature has been estimated to 560 K by the lowest temperature where this model reproduced the peak shape. In the temperature interval between 500 and 560 K the surface can be described as a partly ordered liquid film or as a solid surface with many thermal defects such as interstitials and dislocations [135].

For Pb(111) the Monte-Carlo curve has been created with the assumption of slightly enhanced surface vibration amplitudes and bulk interlayer distances [139]. This curve perfectly describes the measurements all the way up to $T_{\rm m}$, the reason for which surface melting can be excluded for the (111) orientation. Using a cylindrical single crystal a range of 73° of surface orientations around [112] and along the [$\bar{1}$10]-zone could be investigated [139]. The tendency towards surface melting was measured by the areal density of disorderly positioned atoms N. There was absence of positional disorder in a 17° interval around (111) and a significant decrease as the (100) direction is approached suggesting that also Pb(100) does not pre-melt while the other orientations showed a large temperature dependent increase of N, which is a clear signature of surface melting.

The reason for this behavior is the angular dependence of the free energy of the interface between the ordered solid and its vapor, $\gamma_{\rm sv}(\Theta)$, see Fig. 9b). It is useful to define the anisotropic excess surface free energy:

$$\Delta\gamma(\Theta) = \gamma_{\rm sv}(\Theta) - \gamma_{\rm sl}(\Theta) - \gamma_{\rm lv}\,, \tag{5}$$

with the second and third terms being the solid-liquid and liquid-vapor interface free energies, respectively. For surface orientations where this excess energy is larger than zero, the surface gains energy by introducing a fully wetting liquid film, while for $\Delta\gamma(\Theta) < 0$ it is more favorable to keep the interface between solid and vapor up to $T_{\rm m}$. The other way around, surfaces which show no surface melting are wet only incompletely by their own liquid. The droplets forming have external contact angles θ above, and internal contact angles ϕ below the plane defined by the solid surface. These angles give access to the surface free energies by Young's equation:

$$\gamma_{\rm sv} = \gamma_{\rm sl}\cos\phi + \gamma_{\rm lv}\cos\theta\,. \tag{6}$$

The connection between a finite external contact angle in this equation and the above condition of surface melting is seen when assuming $\phi = 0$, then $\theta > 0$ implies $\gamma_{\rm sv} < \gamma_{\rm sl}+\gamma_{\rm lv}$ or $\Delta\gamma < 0$. Typical examples for surfaces showing no surface melting and their respective external contact angles are NaCl(100) with $\theta = 48^\circ$ and Al(111) with $\theta = 18^\circ$ [4].

Coming back to our example of Pb we note that a direct correlation between $\Delta\gamma(\Theta)$ and N can be established, enabling to test the validity of Eq. (5) for all surface orientations and temperatures. Using the measured variation of $\gamma_{\rm sv}(\Theta)/\gamma_{\rm sv}(111)$ together with the absolute value of $\gamma_{\rm sv}(111) = 0.544$ J/m^2 and the empirical rule for the solid-liquid interface free energy $\gamma_{\rm sl} = 0.1\gamma_{\rm sv}$, reproduces the angular dependence of the density of disordered atoms (number of molten layers) at all investigated temperatures. The only fit parameters are the liquid-vapor interface free energy and the reference atomic density. For the first parameter one obtains a value $\gamma_{\rm lv} = 0.501$ J/m^2 close to the average literature value of 0.46 J/m^2. Further, for angles where the measured $\gamma_{\rm sv}(\Theta)/\gamma_{\rm sv}(111)$-curve lies above $\gamma_{\rm sl}(\Theta)/\gamma_{\rm sv}(111)+\gamma_{\rm lv}/\gamma_{\rm sv}(111) = 0.1\gamma_{\rm sv}(\Theta)/\gamma_{\rm sv}(111) + 0.501/544$ pre-melting is expected and where it lies below not, again in full agreement with experiment. From the energies above, the external contact angle of molten Pb droplets on solid Pb(111) near $T_{\rm m}$ can be estimated to 15°.

Figure 14 shows that the surface melting of Pb(110) can be divided into two regimes with different scaling behavior [140]. From 40 K up to 0.3 K below $T_{\rm m}$ the number of molten layers varies as $\ln(T_{\rm m}-T)$ as indicated by the straight line. This is followed by a regime in which the thickness of the liquid layer diverges as $(T_{\rm m}-T)^{-\alpha}$ with $\alpha = 0.315 \pm 0.015$. The two regimes are interpreted as reminiscent of short, respectively, long-range interactions between the lead atoms.

The present choice of metal surfaces as examples of surface melting shall not create the impression that they are more frequently showing this phase transition. As mentioned above, surface melting is observed

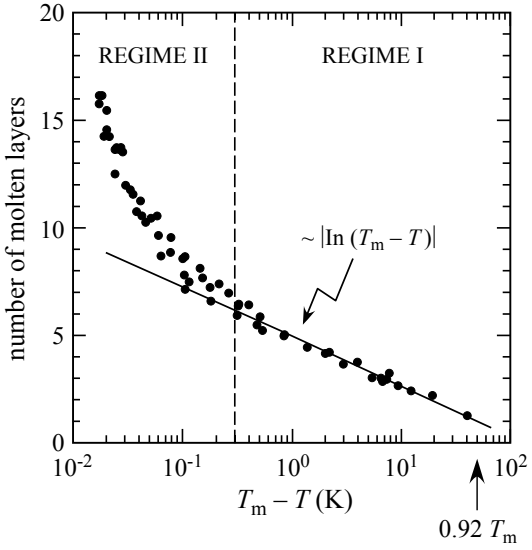

Fig. 14 Half-logarithmic plot of the surface density of molten atoms on Pb(110) derived from MEIS surface peak areas as a function of $T_{\rm m} - T$ [140]. This density can be interpreted as number of molten layers.

on ice, where it also has environmental consequences [141], but also van der Waals crystals such as Ar and Ne layers show the signatures of surface roughening and melting [142, 143]. In these systems there are no short range interactions and therefore they show the power law divergence of the liquid layer thickness only. We also note that each time one steps down in the spatial dimension of the system, the melting temperatures get lower. Similarly to premelting of the 2D boundary of a 3D crystal, there exists premelting of 1D boundaries between domains of a solid surface which melt at much lower temperatures than the surface or bulk melting. On example are the domain walls on the $c(2 \times 8)$ reconstructed Ge(111) surface that melt already at 570 K [144], which is only 47 % of T_{m}. We finally note that surface melting is a very important issue for phase transitions of nanostructures. In these structures the surface, together with its molten layers, represent a significant fraction of the constituent atoms. One of the consequences are the size-dependent melting temperatures observed for Au clusters [145, 146], which could perfectly be reproduced in molecular dynamics simulations [147].

8 Further reading

For *Surface diffusion* we recommend the general overview and tables of diffusion barriers and attempt frequencies given in [7, 19, 148], theory of diffusion is treated in [19], diffusion of adsorbates on metals in [19, 149], of non-metallic adsorbates on metals in [150], and the diffusion of organic molecules on metals in [150, 151]. Step and island dynamics is reviewed in [152]. References to cluster diffusion are [26,153], to surface self-diffusion on oxides [154], and finally for metals on metals we recommend [26,49]. *Thermal Surface Reconstructions* are very well reviewed in [155]. The early theoretical papers on *Surface Roughening* are [156, 157], review papers on the subject are [155, 158], and the following reference is recommended for further reading [159]. The *Surface Melting* of ice is discussed in [141], surface melting in general in [5, 133, 160], and we refer to [161] for an early model predicting surface melting at 73 % T_{m} based on the criterion of mechanical instability. [162] shows for Al surfaces that surface melting is related to the energy cost for the creation of vacancies. The reader is also referred to the literature on dislocation induced melting of pure 2D systems [163–165] and finally to a recent experimental example where this behavior could be observed [166]. Since this overview deals with many surface phase transitions, we also recommend the introduction to phase transitions and critical phenomena by H. E. Stanley [167].

Acknowledgements The author acknowledges C. L. Bandelier for the preparation of the figures.

References

[1] J. E. Avron, L. S. Balfour, C. G. Kuper, J. Landau, S. G. Lipson, and L. S. Schulman, Phys. Rev. Lett. **45**, 814–817 (1980).
[2] S. Balibar, H. Alles, and A. Y. Parshin, Rev. Mod. Phys. **77**, 317 (2005).
[3] T. Zykova-Timan, D. Ceresoli, U. Tartaglino, and E. Tosatti, J. Chem. Phys. **123**, 164701 (2005).
[4] T. Zykova-Timan, U. Tartaglino, D. Ceresoli, and E. Tosatti, Phys. Rev. Lett. **94**, 176105 (2005).
[5] U. Tartaglino, T. Zykova-Timan, F. Ercolessi, and E. Tosatti, Phys. Rep. **411**, 291–321 (2005).
[6] N. Lin, A. Dmitriev, J. Weckesser, J. V. Barth, and K. Kern, Angew. Chem. Int. Ed. **41**, 4779–4783 (2002).
[7] E. G. Seebauer and M. Y. L. Yung, Surface diffusion, in: Physics of Covered Solid Surfaces: I. Adsorbed Layers on Surfaces, edited by H. P. Bonzel, Landolt Börnstein Vol. III/42 Subvolume A, Part 1 (Springer, Berlin, 2001), p. 455.
[8] A. F. Voter and J. D. Doll, J. Chem. Phys. **80**, 5832 (1984).
[9] C. Chen and T. T. Tsong, Phys. Rev. Lett. **64**, 3147 (1990).
[10] E. Ganz, S. K. Theiss, I. Hwang, and J. Golovchenko, Phys. Rev. Lett. **68**, 1567 (1992).
[11] D. C. Senft and G. Ehrlich, Phys. Rev. Lett. **74**, 294 (1995).
[12] T. R. Linderoth, S. Horch, E. Lægsgaard, I. Stensgaard, and F. Besenbacher, Phys. Rev. Lett. **78**, 4978 (1997).
[13] M. Schunack, T. R. Linderoth, F. Rosei, E. Lægsgaard, I. Stensgaard, and F. Besenbacher, Phys. Rev. Lett. **88**, 156102 (2002).

[14] N. Knorr, H. Brune, M. Epple, A. Hirstein, A. M. Schneider, and K. Kern, Phys. Rev. B **65**, 115420 (2002).
[15] J. Repp, F. Moresco, G. Meyer, K. H. Rieder, P. Hyldgaard, and M. Persson, Phys. Rev. Lett. **85**, 2981 (2000).
[16] J. A. Venables and H. Brune, Phys. Rev. B **66**, 195404 (2002).
[17] H. Brune, Creating metal nanostructures at metal surfaces using growth kinetics, in: Handbook of Surface Science, edited by E. Hasselbrink (Elsevier, Amsterdam, 2008), pp. 761–786.
[18] S. Ovesson, A. Bogicevic, G. Wahnström, and B. I. Lundqvist, Phys. Rev. B **64**, 125423 (2001).
[19] R. Gomer, Rep. Prog. Phys. **53**, 917 (1990).
[20] L. J. Lauhon and W. Ho, Phys. Rev. Lett. **85**, 4566 (2000).
[21] R. Gomer, Surf. Sci. **38**, 373–393 (1973).
[22] M. C. Tringides and R. Gomer, Surf. Sci. **155**, 254 (1985).
[23] H. Heinzelmann, F. Watanabe, and G. M. McClelland, Phys. Rev. Lett. **70**, 3611–3614 (1993).
[24] G. Ehrlich, Surf. Sci. **246**, 1–12 (1991).
[25] G. Ehrlich, Appl. Phys. A **55**, 403 (1992).
[26] G. L. Kellogg, Surf. Sci. Rep. **21**, 1–88 (1994).
[27] T. T. Tsong, Atom-probe field ion microscopy (Cambridge University Press, New York, 1990).
[28] Y. W. Mo, Phys. Rev. Lett. **71**, 2923 (1993).
[29] M. Bott, M. Hohage, M. Morgenstern, T. Michely, and G. Comsa, Phys. Rev. Lett. **76**, 1304 (1996).
[30] J. M. Gómez-Rodríuez, J. J. Sáenz, A. M. Baró, J. Y. Veuillen, and R. C. Cinti, Phys. Rev. Lett. **76**, 799 (1996).
[31] H. Brune, J. Wintterlin, R. J. Behm, and G. Ertl, Phys. Rev. B **51**, 13592 (1995).
[32] T. Zambelli, J. Trost, J. Wintterlin, and G. Ertl, Phys. Rev. Lett. **76**, 795 (1996).
[33] B. S. Swartzentruber, Phys. Rev. Lett. **76**, 459 (1996).
[34] D. M. Eigler and E. K. Schweizer, Nature **344**, 524–526 (1990).
[35] M. Ternes, C. P. Lutz, C. F. Hirjibehedin, F. J. Giessibl, and A. J. Heinrich, Science **319**, 1066–1069 (2008).
[36] G. Binnig, H. Fuchs, and E. Stoll, Surf. Sci. **169**, L295–L300 (1986).
[37] M. L. Lozano and M. C. Tringides, Europhys. Lett. **30**, 537 (1995).
[38] J. Ellis and J. P. Toennies, Phys. Rev. Lett. **70**, 2118 (1993).
[39] A. P. Graham, F. Hofmann, J. P. Toennies, L. Y. Chen, and S. C. Ying, Phys. Rev. B **56**, 10567 (1997).
[40] J. W. M. Frenken, J. P. Toennies, and C. Wöll, Phys. Rev. Lett. **60**, 1727–1730 (1988).
[41] M. Breeman and D. O. Boerma, Surf. Sci. **269-270**, 224 (1992).
[42] R. H. Milne, M. Azim, R. Persaud, and J. A. Venables, Phys. Rev. Lett. **73**, 1396 (1994).
[43] A. von Oertzen, H. H. Rotermund, and S. Nettesheim, Surf. Sci. **311**, 322–330 (1994).
[44] J. A. Venables, Philos. Mag. **17**, 697 (1973).
[45] H. Brune, G. S. Bales, C. Boragno, J. Jacobsen, and K. Kern, Phys. Rev. B **60**, 5991 (1999).
[46] J. A. Venables, G. D. T. Spiller, and M. Hanbücken, Rep. Prog. Phys. **47**, 399 (1984).
[47] Y. W. Mo, J. Kleiner, M. B. Webb, and M. G. Lagally, Phys. Rev. Lett. **66**, 1998 (1991).
[48] H. Brune, H. Röder, C. Boragno, and K. Kern, Phys. Rev. Lett. **73**, 1955 (1994).
[49] H. Brune, Surf. Sci. Rep. **31**, 121–229 (1998).
[50] G. L. Nyberg, M. T. Kief, and W. F. Egelhoff, Phys. Rev. B **48**, 14509 (1993).
[51] J. K. Zuo, J. F. Wendelken, H. Dürr, and C. L. Liu, Phys. Rev. Lett. **72**, 3064 (1994).
[52] H. Dürr, J. F. Wendelken, and J. K. Zuo, Surf. Sci. **328**, L527–L532 (1995).
[53] J. J. D. Miguel, A. Sánchez, E. Cebollada, J. M. Gallego, J. Ferrón, and S. Ferrer, Surf. Sci. **189-190**, 1062 (1987).
[54] H. D. Ebinger, H. J. Jänsch, C. Polenz, B. Polivka, W. Preyss, V. Saier, R. Veith, and D. Fick, Phys. Rev. Lett. **76**, 656 (1996).
[55] R. van Gastel, E. Somfai, S. B. von Albada, W. van Saarloos, and J. W. M. Frenken, Phys. Rev. Lett. **86**, 1562 (2001).
[56] R. van Gastel, E. Somfai, W. van Saarloos, and J. W. M. Frenken, Nature **408**, 665 (2000).
[57] M. L. Grant, B. S. Schwartzentruber, N. C. Bartelt, and J. B. Hannon, Phys. Rev. Lett. **86**, 4588–4591 (2001).
[58] R. van Gastel, E. Somfai, S. B. van Albada, W. van Saarloos, and J. W. M. Frenken, Surf. Sci. **521**, 10–25 (2002).
[59] J. B. Hannon, C. Klünker, M. Giesen, H. Ibach, N. C. Bartelt, and J. C. Hamilton, Phys. Rev. Lett. **79**, 2506 (1997).
[60] G. Boisvert and L. J. Lewis, Phys. Rev. B **56**, 7643–7655 (1997).

[61] J. Kolaczkiewicz and E. Bauer, Surf. Sci. **175**, 508–519 (1986).
[62] H. Brune, Metals on metals, in: Physics of Covered Solid Surfaces, edited by H. P. Bonzel, Landolt Börnstein New Series, Group III: Condensed Matter Vol. III/42 Subvolume A, Part 1 (Springer, Berlin, 2001), pp. 217–258.
[63] R. C. Weast, Handbook of Chemistry and Physics (CRC Press, Cleveland, 1978).
[64] T. Fauster, R. Schneider, H. Dürr, G. Engelmann, and E. Taglauer, Surf. Sci. **189/190**, 610–619 (1987).
[65] D. Gorse and J. Lapujoulade, Surf. Sci. **162**, 847 (1985).
[66] E. G. McRae and R. A. Malic, Phys. Rev. B **38**, 13163–13177 (1988).
[67] S. Modesti and A. Santoni, Sol. State Comm. **72**, 315–317 (1989).
[68] A. Mak, K. W. Evans-Lutterodt, K. Blum, D. Y. Noh, J. D. Brock, G. A. Held, and R. J. Birgeneau, Phys. Rev. Lett. **66**, 2002–2005 (1991).
[69] H. Ibach, J. Vac. Sci. Technol. **9**, 713 (1972).
[70] H. Ibach and D. L. Mills, Electron Energy Loss Spectroscopy and Surface Vibrations (Academic Press, New York, 1982).
[71] R. B. Doak and J. P. Toennies, Surf. Sci. **117**, 1 (1982).
[72] D. C. Allan and E. J. Mele, Phys. Rev. Lett. **53**, 826 (1984).
[73] K. Kern, R. David, R. L. Palmer, G. Comsa, and T. S. Rahman, Phys. Rev. B **33**, 4334–4337 (1986).
[74] J. W. Frenken, F. Huussen, and J. F. van der Veen, Phys. Rev. Lett. **58**, 401 (1987).
[75] P. Zeppenfeld, K. Kern, R. David, and G. Comsa, Phys. Rev. Lett. **62**, 63–66 (1989).
[76] B. Poelsema and G. Comsa, Scattering of Thermal Energy Atoms from Disordered Surfaces (Springer Verlag, Berlin, 1989).
[77] S. G. J. Mochrie, Phys. Rev. Lett. **59**, 304–307 (1987).
[78] M. de Nijs, E. K. Riedel, E. H. Conrad, and T. Engel, Phys. Rev. Lett. **55**, 1689 (1985).
[79] M. de Nijs, E. K. Riedel, E. H. Conrad, and T. Engel, Phys. Rev. Lett. **57**, 1279 (1986).
[80] A. P. Baddorf and E. W. Plummer, Phys. Rev. Lett. **66**, 2770–2773 (1991).
[81] G. Armand, D. Gorse, J. Lapujoulade, and J. R. Manson, Europhys. Lett. **3**, 1113–1118 (1987).
[82] I. Avramov and M. Michailov, J. Phys. Cond. Mat. **20**, 295224 (2008).
[83] K. Heinz, G. Schmidt, L. Hammer, and K. Müller, Phys. Rev. B **32**, 6214 (1985).
[84] K. Takayanagi, Y. Tanishiro, M. Takahashi, and S. Takahashi, Surf. Sci. **164**, 367 (1985).
[85] R. J. Hamers, R. M. Tromp, and J. E. Demuth, Phys. Rev. Lett. **56**, 1972 (1986).
[86] H. Huang, S. Y. Tong, W. E. Packard, and M. B. Webb, Phys. Lett. A **130**, 166 (1988).
[87] A. Ichimiya, Surf. Sci. **192**, L893 (1987).
[88] I. K. Robinson, W. K. Waskiewicz, P. H. Fuoss, and L. J. Norton, Phys. Rev. B **37**, 4325 (1988).
[89] I. K. Robinson and E. Vlieg, Extended x-ray reflectivity analysis of si(111)-(7x7), in: Surface X-ray and Neutron Scattering, edited by H. Zabel and I. K. Robinson, Springer Proceedings in Physics Vol. 61 (Springer, Berlin, 1992), pp. 51–55.
[90] F. J. Giessibl, Science **267**, 68 (1995).
[91] L. Olsson, R. Wigren, and R. Erlandsson, Rev. Sci. Instrum. **67**, 2289 (1996).
[92] F. J. Giessibl, S. Hembacher, H. Bielefeldt, and J. Mannhart, Science **289**, 422–425 (2000).
[93] M. A. Lantz, H. J. Hug, R. Hoffmann, P. J. A. van Schendel, P. Kappenberger, S. Martin, A. Baratoff, and H. J. Güntherodt, Science **291**, 2580 (2001).
[94] A. Kahn, Surf. Sci. Rep. **3**, 193 (1983).
[95] N. Osakabe, Y. Tanishiro, K. Yagi, and G. Honjo, Surf. Sci. **109**, 353 (1981).
[96] A. Zangwill, Physics at Surfaces (Cambridge University Press, New York, 1988).
[97] A. R. Sandy, S. G. J. Mochrie, D. M. Zehner, G. Grübel, K. G. Huang, and D. Gibbs, Phys. Rev. Lett. **68**, 2192 (1992).
[98] G. Grübel, K. G. Huang, D. Gibbs, D. M. Zehner, A. R. Sandy, and S. G. J. Mochrie, Phys. Rev. B **48**, 18119–18139 (1993).
[99] M. Bott, M. Hohage, T. Michely, and G. Comsa, Phys. Rev. Lett. **70**, 1489 (1993).
[100] C. Teichert, M. Hohage, T. Michely, and G. Comsa, Phys. Rev. Lett. **72**, 1682 (1994).
[101] R. Pushpa and S. Narasimhan, Phys. Rev. B **67**, 205418 (2003).
[102] J. V. Barth, H. Brune, G. Ertl, and R. J. Behm, Phys. Rev. B **42**, 9307 (1990).
[103] M. Hohage, T. Michely, and G. Comsa, Surf. Sci. **337**, 249 (1995).

[104] R. Kunkel, B. Poelsema, L. K. Verheij, and G. Comsa, Phys. Rev. Lett. **65**, 733 (1990).
[105] T. Michely, M. Hohage, S. Esch, and G. Comsa, Surf. Sci. **349**, L89 (1996).
[106] J. Jacobsen, K. W. Jacobsen, and P. Stoltze, Surf. Sci. **317**, 8 (1994).
[107] W. K. Burton, N. Cabrera, and F. C. Frank, Phil. Trans. A **243**, 299–358 (1951).
[108] H. van Beijeren and I. Nolden, in: Structure and Dynamics of Surface II, edited by W. Schommers and P. von Blanckenhagen (Springer, Berlin, 1987), p. 259.
[109] G. Wulff, Z. Kristallog. **34**, 449 (1901).
[110] J. C. Heyraud and J. J. Métois, Acta Metallurgica **28**, 1789–1797 (1980).
[111] J. C. Heyraud and J. J. Métois, Surf. Sci. **128**, 334–342 (1983).
[112] K. Kern, Thermal dynamics of (110) fcc metal surfaces, in: Surface X-Ray and Neutron Scattering, edited by H. Zabel and I. K. Robinson, Springer Proceedings in Physics Vol. 61 (Springer, Berlin, 1992), pp. 69–71.
[113] S. G. J. Mochrie, D. M. Zehner, B. M. Ocko, and D. Gibbs, Phys. Rev. Lett. **64**, 2925–2928 (1990).
[114] D. Gibbs, B. M. Ocko, D. M. Zehner, and S. G. J. Mochrie, Phys. Rev. B **42**, 7330–7344 (1990).
[115] B. M. Ocko, D. Gibbs, K. G. Huang, D. M. Zehner, and S. G. J. Mochrie, Phys. Rev. B **44**, 6429–6443 (1991).
[116] D. L. Abernathy, S. G. J. Mochrie, D. M. Zehner, G. Grübel, and D. Gibbs, Phys. Rev. B **45**, 9272–9291 (1992).
[117] R. Miranda, E. V. Albano, S. Daiser, G. Ertl, and K. Wandelt, Phys. Rev. Lett. **51**, 782–785 (1983).
[118] F. Calleja, M. G. C. Passeggi, J. J. Hinarejos, A. L. V. de Parga, and R. Miranda, Phys. Rev. Lett. **97**, 186104 (2006).
[119] R. Otero, A. L. V. de Parga, and R. Miranda, Phys. Rev. B **66**, 115401 (2002).
[120] I. K. Robinson, E. Vlieg, H. Hornis, and E. H. Conrad, Phys. Rev. Lett. **67**, 1890–1893 (1991).
[121] I. K. Robinson, E. Vlieg, and K. Kern, Phys. Rev. Lett. **63**, 2578–2581 (1989).
[122] E. H. Conrad, R. M. Aten, D. S. Kaufmann, L. R. Allen, T. Engel, M. de Nijs, and E. K. Riedel, J. Chem . Phys. **84**, 1015 (1986).
[123] E. H. Conrad, R. M. Aten, D. S. Kaufmann, L. R. Allen, T. Engel, M. de Nijs, and E. K. Riedel, J. Chem . Phys. **85**, 4756 (1986).
[124] J. Lapujoulade, Surf. Sci. **178**, 406 (1986).
[125] F. Fabre, D. Gorse, J. Lapujoulade, and B. Salanon, Europhys. Lett. **3**, 737–743 (1987).
[126] E. H. Conrad, L. R. Allen, D. L. Blanchard, and T. Engel, Surf. Sci. **187**, 265 (1987).
[127] K. S. Liang, E. B. Sirota, K. L. D'Amico, G. J. Hughes, and S. K. Shina, Phys. Rev. Lett. **59**, 2447 (1987).
[128] F. Fabre, B. Salanon, and J. Lapujoulade, Sol. State Comm. **64**, 1125–1129 (1987).
[129] J. Villain, D. R. Grempel, and J. Lapujoulade, J. Phys. F **15**, 809 (1985).
[130] A. R. Ubbelohde, The Molten State of Matter (Wiley, New York, 1978).
[131] J. S. Langer, Rev. Mod. Phys. **52**, 1 (1980).
[132] F. A. Lindemann, Phys. Z. **14**, 609 (1910).
[133] J. G. Dash, Contemp. Phys. **30**, 89–100 (1989).
[134] J. Daeges, H. Gleiter, and J. H. Perepezko, Phys. Lett. A **119**, 79–82 (1986).
[135] J. W. M. Frenken and J. F. van der Veen, Phys. Rev. Lett. **54**, 134 (1985).
[136] H. H. Andersen and J. F. Ziegler, The Stopping and Ranges of Ions in Matter (Pergamon, New York, 1977).
[137] J. W. Frenken, P. M. Marée, and J. F. van der Veen, Phys. Rev. B **34**, 7506 (1986).
[138] B. Pluis, A. W. D. van der Gon, J. F. van der Veen, and A. J. Riemersma, Surf. Sci. **239**, 265–281 (1990).
[139] B. Pluis, A. W. van der Gon, J. W. Frenken, and J. F. van der Veen, Phys. Rev. Lett. **59**, 2678 (1987).
[140] B. Pluis, T. N. Taylor, D. Frenkel, and J. F. van der Veen, Phys. Rev. B **40**, 1353 (1989).
[141] J. G. Dash, H. Fu, and J. S. Wettlaufer, Rep. Prog. Phys. **58**, 115–167 (1995).
[142] D. M. Zhu and J. G. Dash, Phys. Rev. Lett. **57**, 2959–2962 (1986).
[143] D. M. Zhu and J. G. Dash, Phys. Rev. Lett. **60**, 432–435 (1988).
[144] R. M. Feenstra, A. J. Slavin, G. A. Held, and M. A. Lutz, Phys. Rev. Lett. **66**, 3257 (1991).
[145] P. Buffat and J. P. Borel, Phys. Rev. A **13**, 2287–2298 (1976).
[146] J. P. Borel, Surf. Sci. **106**, 1–9 (1981).
[147] F. Ercolessi, W. Andreoni, and E. Tosatti, Phys. Rev. Lett. **66**, 911–914 (1991).
[148] M. C. Tringides (ed.), Surface Diffusion – Atomistic and Collective Processes, NATO Advanced Science Institute Series B: Physics, Vol. 360 (Plenum Press, New York, 1997).
[149] H. P. Bonzel, Surface diffusion on metals, in: Physics of Solid Surfaces, edited by O. Madelung, Landolt Börnstein New Series, Group III: Condensed Matter Vol. III/26 (Springer, Berlin, 1993), pp. 717–747.

[150] J. V. Barth, Surf. Sci. Rep. **40**, 75 (2000).
[151] F. Rosei, M. Schunack, Y. Naitoh, P. Jiang, A. Gourdon, E. Lægsgaard, I. Stensgaard, C. Joachim, and F. Besenbacher, Prog. Surf. Sci. **71**, 95–146 (2003).
[152] M. Giesen, Prog. Surf. Sci. **68**, 1–153 (2001).
[153] P. Jensen, Rev. Mod. Phys. **71**, 1695–1735 (1999).
[154] M. A. Henderson, Surf. Sci. **419**, 174–187 (1999).
[155] M. Bernasconi and E. Tosatti, Surf. Sci. Rep. **17**, 363–422 (1993).
[156] H. van Beijeren, Phys. Rev. Lett. **38**, 993–996 (1977).
[157] S. T. Chui and J. D. Weeks, Phys. Rev. Lett. **40**, 733–736 (1978).
[158] J. Lapujoulade, Surf. Sci. Rep. **20**, 195–249 (1994).
[159] E. H. Conrad and T. Engel, Surf. Sci. **299/300**, 391 (1994).
[160] J. F. van der Veen, Surf. Sci. **433**, 1–11 (1999).
[161] L. Pietronero and E. Tosatti, Sol. State Comm. **32**, 255–259 (1979).
[162] P. Stoltze, J. K. Nørskov, and U. Landman, Phys. Rev. Lett. **61**, 440–443 (1988).
[163] J. M. Kosterlitz and D. J. Thouless, J. Phys. C: Solid State Phys. **6**, 1181–1203 (1973).
[164] B. I. Halperin and D. R. Nelson, Phys. Rev. Lett. **41**, 121–124 (1978).
[165] D. R. Nelson and B. I. Halperin, Phys. Rev. B **19**, 2457–2484 (1979).
[166] N. N. Negulyaev, V. S. Stepanyuk, L. Niebergall, P. Bruno, M. Pivetta, M. Ternes, F. Patthey, and W. D. Schneider, Phys. Rev. Lett. **102**, 246102 (2009).
[167] H. E. Stanley, Introduction to Phase Transitions and Critical Phenomena (Oxford University Press, New York, 1971).

